







RESEARCH ARTICLE | APRIL 01 2024

An incoherent Thomson scattering system for measurements near plasma boundaries

Jean Luis Suazo Betancourt   ; Julian Lopez-Urcochea  ; Naia Butler-Craig  ; Adam M. Steinberg  ; Mitchell L. R. Walker 

 Check for updates

Rev. Sci. Instrum. 95, 043001 (2024)

<https://doi.org/10.1063/5.0184358>

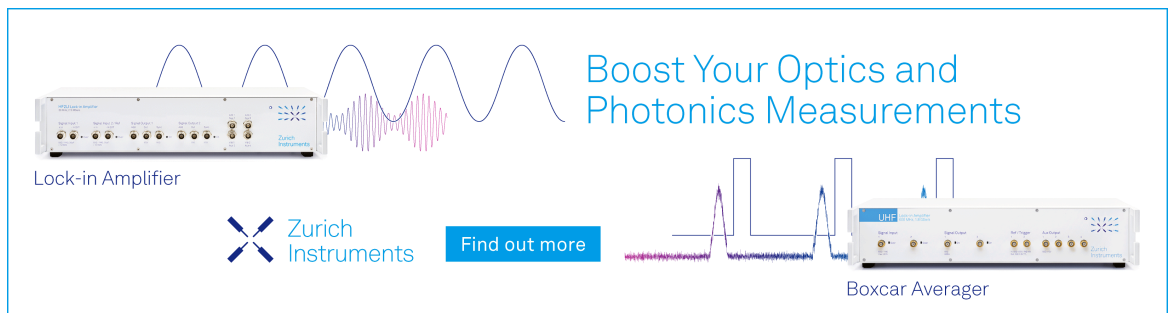


View Online




Export Citation

Boost Your Optics and Photonics Measurements



Lock-in Amplifier

 Zurich Instruments

[Find out more](#)

Boxcar Averager

An incoherent Thomson scattering system for measurements near plasma boundaries

Cite as: Rev. Sci. Instrum. 95, 043001 (2024); doi: 10.1063/5.0184358

Submitted: 25 October 2023 • Accepted: 13 March 2024 •

Published Online: 1 April 2024



View Online



Export Citation



CrossMark

Jean Luis Suazo Betancourt,^{a)} Julian Lopez-Uricoechea, Naia Butler-Craig, Adam M. Steinberg,
and Mitchell L. R. Walker

AFFILIATIONS

School of Aerospace Engineering, Georgia Institute of Technology, Atlanta, Georgia 30318, USA

^{a)} Author to whom correspondence should be addressed: jlsb3@gatech.edu

ABSTRACT

Laser Thomson scattering (LTS) is a minimally invasive measurement technique used for determining electron properties in plasma systems. Sheath model closure validation requires minimally invasive measurements of the electron properties that traverse the boundaries between the bulk plasma, the presheath, and the plasma sheath. Several studies have probed the radial properties along the surface of discharge electrodes with laser-based diagnostics and electrostatic probes. These measurements provide valuable insight into the electron properties in this dynamic region. However, sheath model calibration requires plasma property measurements perpendicular to plasma bounding surfaces, in this case, along the electrode normal vector between discharge electrodes. This work presents the development of a discharge plasma cell and laser Thomson scattering system with a measurement volume step of 1 mm normal to plasma bounding surfaces. The laser Thomson scattering measurements are made between a set of discharge electrodes separated by ~ 25 mm that are used to generate a pulsed argon plasma. The spatial distribution of electron temperature and density is measured at several discharge voltages between 8 and 20 kV at a pressure of 8 Torr-Ar. It is determined that the system is statistically stationary and resembles a classic DC discharge plasma. The results are some of the first laser diagnostic-based “between electrode” measurements made along the plasma bounding electrode normal vector. A one-dimensional sheath model is applied to determine the near cathode electron properties, and it is determined that the edge of the presheath is probed in the high-voltage cases. As the lengths of the presheath and sheath decrease with decreasing voltage, the region recedes below the closest probed point to the cathode. To improve the performance of the diagnostic, the step size of the interrogation volume should decrease by an order of magnitude from 1 mm to less than 100 μm , and the data acquisition strategy should be revised to increase the signal-to-noise ratio.

Published under an exclusive license by AIP Publishing. <https://doi.org/10.1063/5.0184358>

I. INTRODUCTION

Plasma sheaths are non-quasineutral structures that form at the Debye-shielded boundaries of any confined plasma and play an important role in the plasma boundary interactions.¹ There are generally two types of external boundary conditions. The first occurs when the potential is externally enforced and is typically seen at conducting electrodes, where a net current can be drawn. The second occurs at a zero net current boundary condition, also known as the floating boundary condition, and is typically seen at the non-conducting boundaries of dielectric materials in contact with a plasma. The sheath at a conducting boundary held at a negative potential relative to the bulk plasma potential is referred to as an ion-rich sheath or simply an ion sheath. Similarly, a sheath at the boundary held at a positive potential relative to the bulk plasma potential is referred to as an electron-rich sheath or electron sheath.

In a classic floating DC discharge, an ion sheath forms at the cathode and an electron sheath forms at the anode.

Ion sheath measurements with electrostatic probes, specifically emissive probes, show good agreement with the Child–Langmuir (CL) derivations for potential variations in the transition from the bulk plasma to the sheath via a presheath, with the measurements showing slightly larger than expected sheaths.² Several other studies have demonstrated the applicability of the CL laws to ion sheaths in DC discharges.³

Electron sheaths, on the other hand, are not as well understood, exhibiting potential dip structures that are not predicted by the CL theory when the anode is transitioned from being mostly insulated (via ceramic) to fully conducting.² This transition was confirmed via a DC discharge experiment with conducting and insulated walls, where plasma measurements were taken via a Langmuir probe.⁴ In

addition, a study using a segmented anode that could vary its effective surface area concluded that the size of the anode plays a role in the transition from an electron-rich to an ion-rich sheath.⁵ From these studies, it is clear that electrical boundary conditions, as well as the relative size of the electrodes with respect to each other and the plasma, play a role in electron and ion sheath transitions.

A study of the theory of sheaths and presheaths concluded that the reason transitions between electron-rich and ion-rich sheaths, as well as other aforementioned discrepancies with experimental data, were not predicted is because electron-rich sheath models presumed a random electron flux to the anode; this assumption is insufficient in describing the flux of electrons from the bulk plasma to the electron sheath at the anode via its presheath.⁶ As a result, electron sheaths were predicted via PIC simulations to be about twice as large as previous estimates.²

From these studies, it is clear that electrical boundary conditions, as well as the relative size of the electrodes with respect to each other, play a role in electron and ion sheath transitions. Electron and ion sheath models give predictions of the size of sheath structures as functions of bulk plasma properties and electrode boundary conditions with respect to the bulk plasma.^{6,7} However, to date, spatially resolved measurements along the electrode normal vectors are scarce and have not confirmed these structures in confined plasmas, such as electrode discharges. Such measurements would inform sheath models that are critical for closures in larger simulations, such as those used to simulate Hall effect thrusters.⁸

First-order models for the sheath and presheath spatial structures and length scales rely on the assumption of a bulk plasma whose extent is much larger than that of the sheath and presheath length scales. This assumed large extending bulk plasma allows the sheath and presheath models to rely on the bulk plasma properties as predictors for the sheath and presheath length scales and plasma potential profiles. However, previous electron property measurements in such discharges have not confirmed the existence of such a bulk plasma between the electrodes. In addition, experimental studies have not probed close enough to the electrodes with a minimally invasive diagnostic in such a way as to spatially resolve the properties and gain more insight into the bulk plasma presheath boundary. Moreover, experimental parametric studies on the effect of external boundary conditions on these structures have not been performed.

Laser Thomson scattering (LTS) is an alternative to electrostatic probes that can be minimally invasive and used for measuring plasma properties in the vicinity of these conducting boundaries with high-spatial resolution. A minimally invasive alternative is desirable as it is well understood that the presence of electrostatic probes affects the local potential structure and particle densities in the plasma. Thus, in the vicinity of a sheath, perturbations to the potential structure will affect the estimates of the size of the sheath and presheath. To date, many LTS studies have been conducted in low-pressure discharges.⁹⁻¹⁶ Most recently, a temporally and radially resolved investigation in an ms-pulsed DC discharge was conducted.¹⁷ However, spatially resolved plasma property measurements perpendicular to the plasma bounding surfaces are lacking in the literature. These measurements are critical for informing plasma sheath simulations.

This paper presents a discharge plasma cell and LTS system capable of probing perpendicular to the plasma bounding electrodes for studying the bulk plasma-presheath boundary. The ability to

probe perpendicular to the surface of the electrodes is a by-product of the physical construction of the system. The distance required to probe into the sheath and presheath regions is determined after comparing the data at the closest probed point to a sheath and presheath plasma model. Furthermore, the diagnostic can measure with a spatial resolution typically inaccessible to electrostatic probes. In situations with sufficient signal-to-noise ratios, the system outlined below provides a diagnostic whose signal inversion requires fewer assumptions than electrostatic probes. This, coupled with the diagnostic system's minimally invasive nature, allows for accurate measurements of the plasma properties approaching plasma boundaries that are more reliable than electrostatic probes. We use this system to investigate a plasma bounding sheath model in a simple two-electrode discharge. The results can be used to enhance the fidelity of models for more complex real-world plasma devices.

II. DISCHARGE PLASMA CELL

A. Discharge cell construction

A custom vacuum test cell was constructed from off-the-shelf and custom CF and KF equipment. The front view of the cell is shown in Fig. 1. The main body of the cell, which houses the test section, is a Kurt J. Lesker stainless steel 4.5 in. CF six-way cross tube. Vertically, in the $\pm y$ directions, two reducing nipples connect the main body of the cell to the two bellows UHV Design LSM38-50-H-ES flanged linear translation feedthroughs. The linear feedthroughs have 50 mm of total travel, driven by a rotating shaft gear. These translation feedthroughs allow movement of the electrodes relative to the body of the cell. The main power feedthroughs are 3/4 in. diameter isolated copper feedthroughs. Being too short to reach the test section, they were extended via 3/4 in. 110 copper rods and shielded with 3/4 in. ID alumina sleeves. The electrodes at the end of the copper rods are 1/2 in. thick, 24 mm diameter stainless steel discs. The alumina cladding shielded the copper from the plasma to avoid vaporization and increase the electrical isolation between the floating electrodes to the grounded vacuum cell walls.

To reduce laser reflections during the LTS experiments described below, baffles were machined and press fit on both sides of the test section in the x directions (the laser propagation direction). The inner diameter of the baffles was chosen to be as small as possible without clipping the beam. These baffles also defined the optical axis for laser propagation. In the $\pm z$ directions, two high transmission viewports provided optical access to the test section for light collection.

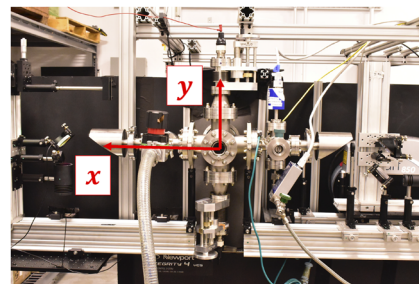


FIG. 1. Front view of the plasma cell. Here, z follows the right-hand rule.

In the $-x$ direction, a 2.75 in. CF six-way cross tube housed the pressure measurement and mass flow devices. Two capacitance manometers—one MKS XCG-BT-FB-1 with a range of 1000 to 1 Torr and one MKS ACG-HT-2-1 with a range of 10 Torr to 1 mTorr—were used to measure the pressure in the vacuum cell over the desired range of 760 Torr to 100 mTorr; the laser measurements over this pressure range were used to collect rotational laser Raman scattering (LRS) data. With modern laser line filtering elements, LRS is the preferred method for calibrating the LTS measurements for the absolute number density.^{18–22} An MKS GE50A013502RMV020 mass flow controller, with a maximum flow rate of 500 sccm, was used to control the neutral gas input to the system. The manometers and mass flow controller were tied to a National Instruments NI-USB-6211, which was controlled via a custom LabVIEW VI for pressure control. Finally, a reducing nipple was coupled to a custom Torr Scientific NSQ1462-25 KF50 Brewster window with a 25 mm clear aperture onto the cell.

In the x direction, a four-way cross interfaced to a second Brewster window at the laser beam exit. In addition, a Kurt J Lesker C33355000 KF25 diaphragm valve was interfaced to the cell. This valve sealed the cell from the Alcatel Adixen 2010SD rotary vane vacuum pump and also acted as a variable conductance valve to modulate the pumping speed. The pump and valve were connected via a 1 in. ID, 6-foot long PVC tube. At the working pressure of 2.1×10^3 mBar, the pump's throughput is rated as 2.97 l/s or 178×10^3 ccm. Conductance loss calculations estimated the test section pumping throughput to be 154×10^3 ccm. A throughput of up to 100×10^3 ccm for pressures at 100 Torr- N_2 was necessary to maintain the pressure during the collection system calibrations via Raman scattering. This would have required an impractically sized mass flow controller and flow rates into the cell. Instead, the diaphragm valve was used to decrease the conductance by restricting the orifice size at the cell. In this way, we can reach the desired pressures by filling the cell with the flow controller open and the diaphragm valve closed and then actuate the valve in order to re-establish pumping and allow for fine control of the pressure via the pressure control loop.

Figure 2 shows a diagram of the electrical configuration of the vacuum test cell and electrodes. The body of the vacuum cell was tied electrically to the surface of the optical table, which was intentionally tied to the ground. The power feedthroughs isolated the discharge electrodes from the vacuum test cell, ensuring that their base configuration was floating with respect to the vacuum cell. Between the vacuum cell anode and the power supply anode terminal, a 1 Ω , 2500 W resistor was placed in series. The voltage across the electrodes was driven by an Eagle Harbor NSP-120-20F ns-pulsed power supply with a 10 kHz maximum repetition rate and ground-isolated output electrodes.

B. Pulsed plasma current and repeatability

The spatially resolved LTS data described below were acquired over a two-hour test period under each plasma operating condition, which was set by the number of accumulated laser pulses required for a good signal-to-noise ratio and a number of spatial measurement locations. To confirm that the plasma pulse was repeatable and statistically stationary over an LTS measurement window, a total of 100 plasma current signals were taken over a two-hour period

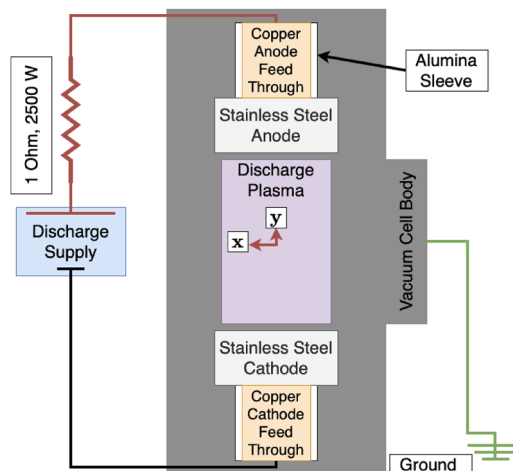


FIG. 2. Vacuum cell electrical configuration and discharge cell physical layout. The interrogation laser beam propagates parallel to x . The normal vectors for the cathode and anode are $+y$ and $-y$, respectively.

using a CP030 current clamp connected to a Teledyne Lecroy Wave-Pro 404HD oscilloscope. Figure 3 shows the temporal profile from each plasma pulse as thin lines, with the ensemble average profile shown as a thicker line. Four different voltages were studied, evenly spaced from 8 to 20 kV, with corresponding peak currents of 8.1, 13.1, 18.5, and 23.2 A, respectively. The maximum value of the difference between the individual pulses and the ensemble average over all conditions is less than 0.5%, indicating that the plasma is repeatable and stationary. In addition, to monitor stationarity during the LTS acquisition, a single discharge current signal was taken for each spatially probed LTS data point; these showed similar behavior to Fig. 3.

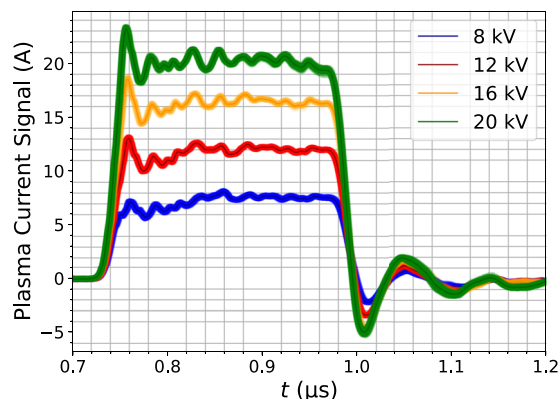


FIG. 3. Individual and averaged discharge current signals at several discharge voltages. Individual scope lines are plotted with thin soft colored lines, and the average scope signal is plotted with a dark colored line.

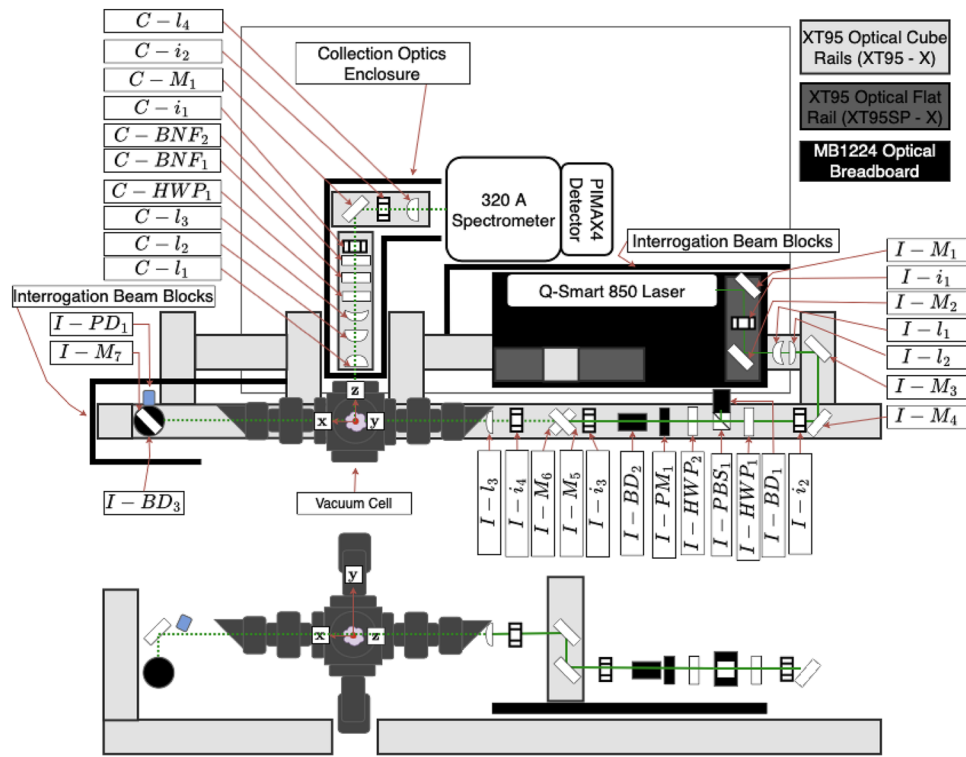


FIG. 4. Top and front of the vacuum cell relative to the interrogation and collection systems. M , i , l , PBS , HWP , BD , PD , PM , F , and BNF are acronyms for mirrors, irises, lenses, polarizing beam splitter cubes, half wave plates, beam dumps, photodiodes, power meters, and Bragg notch filters, respectively. I - and C - indicate interrogation and collection, respectively, the axes to which the optical element corresponds.

III. INCOHERENT THOMSON SCATTERING SYSTEM

The spatially resolved measurements of the plasma electron properties were made using incoherent LTS, calibrated for the absolute number density based on rotational LRS. The expected plasma properties (confirmed below) were in the range $n_e = 1 \times 10^{16} - 1 \times 10^{18} \text{ m}^{-3}$ and $T_e = 1 - 50 \text{ eV}$. Following the calculations in Secs. III E and III F of Ref. 20—which consider heating via inverse Bremsstrahlung, ponderomotive density perturbation, and photon ionization—perturbations to the plasma were determined to be minimal under these conditions. Figure 4 shows the system’s master optical diagram, outlining the interrogation beam path and the collection beam path, with a description of the optical parameters presented in Table I.

A. Optical setup

The interrogation laser beam for the LTS and LRS measurements was generated using a Quantel Q-Smart 850 Nd:YAG laser (10 Hz, 532 nm, 200 mJ/pulse, 8 mm beam diameter). Repeatable alignment of the beam along various optical axes was achieved using irises, $I - i_i$, placed at multiple locations. $I - i_1$ to $I - i_3$ were self-consistently aligned to define the optical axis up to $I - M_5$ and $I - M_6$. $I - i_4$ was aligned to the height of the vacuum cell to define the vacuum cell-centered optical axis at that height. The 8 mm diameter beam was expanded to 16 mm using a two-to-one beam

TABLE I. Interrogation beam optical parameters.

Element	Aperture (mm)	Focal length (mm)
Laser
$I - M_i$	50.8	...
$I - BD_i$	20.0	...
$I - PM_1$	20.0	...
$I - i_i$	Variable	...
$I - HWP_i$	20.0	...
$I - PBS_1$	25.4	...
$I - l_1$	25.4	-50
$I - l_2$	25.4	100
$I - l_3$	25.4	400

expander that comprised of lenses $I - l_1$ and $I - l_2$, after which mirrors $I - M_3$ and $I - M_4$ steered the beam on the main leg of the interrogation beam optical axis. The laser energy to the test section was controlled using a half wave plate $I - HWP_1$ and polarizing beam splitter $I - PBS_1$, arranged such that the S-polarized light (parallel \mathbf{z}) was reflected into a beam dump, $I - BD_1$, and the P-polarized light was transmitted.

Then, a second half wave plate $I - HWP_2$ tuned the polarization to maximize the scattering signal in the detector direction once the

beam was in the vacuum cell. The beam energy was measured after $I - HWP_2$ using a Gentec UP19K-15S-H5-D0 power meter $I - PM_1$ placed on a flip mount for easy removal from the beam path. $I - BD_2$ was also placed on a flip mount, blocking the beam before continuing down the optical beam path. $I - M_5$ and $I - M_6$ steer the beam up to the optical axis, defined by the center of the cell along the x direction. Then, $I - l_3$ focuses the beam onto the test section inside the cell. The image of the beam waist, after normalization by the system magnification of two, was about $75 \mu\text{m}$ wide by 2.5 mm long. Given that the beam was propagating along x and the electrode normal vectors are parallel to y , the effective spatial resolution in the electrode-normal direction is $75 \mu\text{m}$.

The mirror $I - M_7$ directed the beam vertically along y , after the cell and prior to the final beam dump, minimizing the stray light traveling toward the detector. Photodiode $I - PD_1$ was used to monitor the timing. The shot-to-shot laser energy variation was less than 5% over the time span of a 3000 laser-shot accumulated spectrum (see below for a description of the collection system). Given the linear nature of LTS, the average laser pulse energy for an accumulation was used in the LTS signal inversion. The time lag of light propagation from the test section to $I - PD_1$ was expected to be on the order of the temporal jitter of the laser; the detector gate duration was sufficient that these did not affect light collection.

Light scattered from electrons and ions at the beam waist was relayed, filtered, and then, focused into the spectrograph via the collection optical system. The light collection system was carefully designed to maximize the signal passed to the detector. The collection system optical diagram is shown in Fig. 5, along with the ideal ray optic matrices used in the thin lens optimization of the system's

collection solid angle; various other parameters of the optics are presented in Table II.

The scattered light is collected by $C - l_1$, relayed via $C - l_2$ to create a one-to-one image, and collimated via $C - l_3$. The light is then transmitted through $C - HWP_1$, rotating the polarization such

TABLE II. Optical parameters of the collection system. The separation distance, δz_i , is shown in Fig. 5.

Element	D or ID (mm)	f or distance (mm)
$\Delta z_{l_1}/\text{beam}$...	200
$C - l_1$	50.8	200
$\Delta z_{l_2}/l_1$...	25
$C - l_2$	50.8	200
$\Delta z_{l_3}/l_2$...	150
$C - l_3$	25.4	-50
$\Delta z_{HWP_1}/l_3$...	25
$C - HWP_1$	25.4	...
$\Delta z_{BNF_1}/HWP_1$...	25
$C - BNF_1$	12.5	...
$\Delta z_{BNF_2}/BNF_1$...	25
$C - BNF_2$	12.5	...
$\Delta z_{l_4}/BNF_2$...	75
$C - l_4$	25.4	100
$\Delta z_{\text{slit}}/l_4$...	100

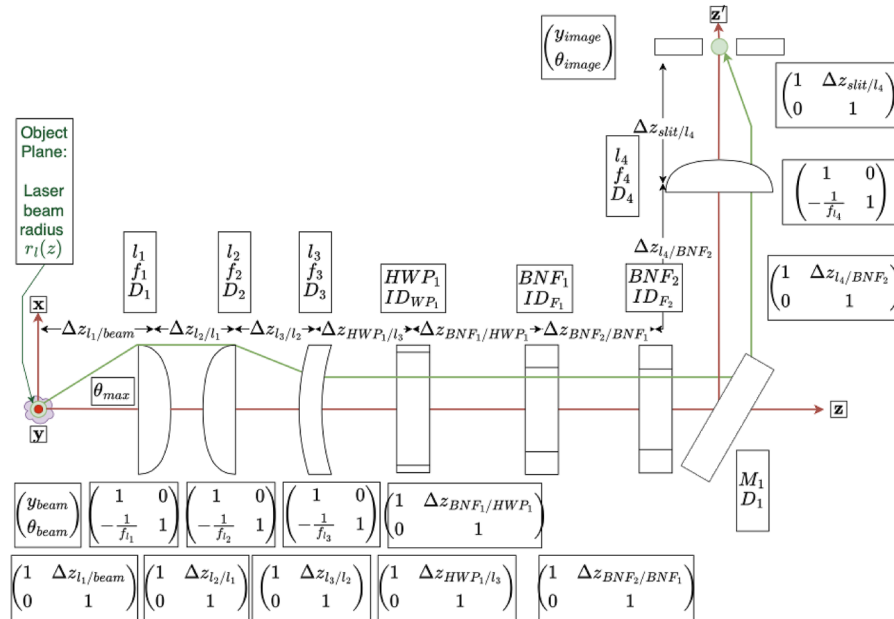


FIG. 5. Collection system's optical diagram. The optical elements, their relative spacing, their individual ray matrices, and their relative spacing ray matrices are labeled. The optimized collection parameters are presented in Table II. In the physical implementation of the system, collimated light is incident onto the curved surface of the lenses to minimize the introduction of spherical aberrations.

that it is appropriate for dispersion using the spectrometer grating; the half wave plate increases the signal intensity by about 5%–10% through this polarization matching. Immediately after $C - HW P_1$, the collected and collimated rays passed through two OptiGrate BNF-532-OD4 laser line volume Bragg grating notch filters, which have OD4 blocking when properly aligned. These filters reduce the light reflected/scattered toward the detector from the solid surfaces and the ions/neutrals. This unwanted light can be orders of magnitude greater than the desired signal from the electrons but is less Doppler-broadened than the electron-scattered light. The removal of this portion of the scattering spectrum allows better signal inversion for electron properties, using the broadened portion of the scattering spectrum from the electrons that is outside the filter blocking range. The sizing of our collection elements used the inner diameter of the smaller of our two BNF filters, ID_{BNF_1} , as the limiting clear aperture since it is the smallest of the two BNF filters. The spectrally filtered light was then steered with mirror $C - M_1$ through the $C - l_4$ lens to create a sharp image of the beam waist section on the spectrograph slit plane.

The collection optics set the collection solid angle, magnification, and minimum spatial resolution of the measurement. In order to use the entire solid angle acquired via the high $f/\#$ collection lens $C - l_1$, the limiting aperture of the full collection system must be the same as $C - l_1$, while also ensuring that all of the rays pass through the clear aperture of $C - BNF_1$. In order to maintain good spatial and spectral resolution, the magnification through our optical system is desired to be no more than two. The vacuum test cell set the minimum focal length to $f = 200$ mm, and the maximum achromatic lens diameter that led to a reasonable amount of light collected without increasing the stray light collection was $D_l = 50.8$ mm. The focal length of 200 mm allowed simultaneous optimization for a system magnification of less than two, collimated ray height at the BNFs of less than their clear aperture, and matching the spectrometer's $f/4.6$, all while satisfying the Helmholtz–Lagrange invariant through the system. In addition, the four-lens collection system allowed for adequate relative sizing of the BNF rejection ring image with respect to the beam waist image on the spectrometer slit plane.

The spectrograph comprised of a Princeton Instruments ISOPLANE-320A spectrometer and a PM4-1024i-HB-FG-18-P46 PIMAX4 camera. The spectrograph entrance plane contained two slits; the slit that is built into the spectrometer ($slit_1$ with an opening of 150 μm) and a secondary slit ($slit_2$ with an opening of 5 mm) that is placed perpendicular to the first slit. The spectrograph was turned 90°, such that $slit_1$ is parallel to the propagation of the beam path along x , making $slit_2$ parallel to y . A 2400 l/mm grating was used to disperse the incoming light. For the experiments conducted here, the intensifier gate was set to 8 ns, and 3000 individual laser pulses were accumulated before reading out the sensor. The timing between the pulsed plasma, laser pulse, and intensifier gate was controlled using a Berkeley Nucleonics BNC-577-8C delay generator.

B. Laser Raman and Thomson scattering models

Thomson scattering is the elastic scattering of incident radiation from unbounded electrons and ions. Here, our focus is on the unbound electrons. The light scattered from the electrons is spectrally broadened and shifted due to their random and bulk motion, respectively, to a greater extent than the slower moving ions, and the

light scattered from the ions is removed using the BNFs. Hence, our LTS signal provides a direct measurement of the electron velocity distribution function (EVDF) and bulk electron velocity along the scattering wave vector, both of which are important for 2D model verification. Furthermore, given a proper system calibration, the amplitude of the LTS spectrum also indicates the electron number density.

Rotational LRS is the preferred technique for calibrating LTS because rotational Raman scattering is less susceptible to interference at the laser wavelength, e.g., due to surface reflections, than alternatives such as Rayleigh scattering.^{18,19} Given that rotational Raman scattering is inelastic, interference from the laser can be mitigated with a filter.

Both Raman and Thomson scattering model equations, superscripted with “R” and “T,” respectively, feature a large number of variables, some of which are deemed “quantities of interest” (QoI), denoted by vector \mathbf{x} , and others that are “nuisance parameters,” i.e., variables that affect the QoI but are not of primary interest, denoted by θ . In this context, nuisance parameters are measured or inferred through the complete signal inversion process but are not directly included in the inversion of interest.

The shape of the LRS spectrum is dependent on the neutral gas temperature, T_g , and the intensity is proportional to the gas number density, n_g , which depends on T_g and the pressure, p_g . More specifically, the LRS scattering intensity in units of counts per nm at wavelength λ , produced by monochromatic incident light at the wavelength λ_i and intensity E_i , is

$$P_\lambda^R(\mathbf{x}^R, \theta^R) = \eta \frac{\lambda_i}{hc} \Delta\Omega L E_i n_g(T_g, p_g) \sum_j \frac{\partial \sigma^R}{\partial \Omega_j} S_\lambda^R(\lambda_j, \tau), \quad (1)$$

where η is the collection efficiency of the optical system, $\Delta\Omega$ is the solid angle of collection, L is the length of the probe volume, and λ_i/hc is the conversion from incident energy to photon counts. The differential Raman scattering cross section of the gas is $\partial \sigma^R / \partial \Omega$ and S_λ^R is the spectral distribution function. The details of the Raman sub-functions are presented in the Appendix of Ref. 23.

For Raman scattering, the QoI are the variables that affect the center, width, maximum peak intensity, and spread of the Raman spectrum. Because the Raman spectrum is linear in the neutral gas pressure, which is measured using a pressure gauge, this is the nuisance parameter in the Raman model equation. The Raman QoI and nuisance parameters are

$$\mathbf{x}^R = [T_g, \tau, \eta, \lambda_i]^\top \quad \text{and} \quad \theta^R = p_g. \quad (2)$$

Given the known laser, gas, and spectral parameters, the measurement of P_λ^R from neutral gases can be used to determine η and λ_i for subsequent use in the LTS measurements. Note that fitting λ_i is necessary, even if the laser wavelength is known to good accuracy, since any misalignment of the image of the object on the slit plane with respect to the column of pixels that define the center wavelength can result in an incorrect inference of the bulk shift. Therefore, these QoI from the Raman inference are nuisance parameters in the Thomson inference. At a given measured neutral gas pressure, a least squares fit is used to determine \mathbf{x}^R . Then, λ_i and η are used as constant inputs to the LTS least squares inversion to solve for the Maxwellian electron properties \mathbf{x}^M , as defined below.

The variance in the measured parameters is calculated by estimating the covariance matrix using the Jacobian output from the nonlinear least squares algorithm.²⁴ This covariance matrix is then used to calculate the 95% confidence interval.

Thomson scattering signals are described by

$$P_{\lambda}^T(\mathbf{x}^T, \boldsymbol{\theta}^T) = \eta \frac{\lambda_i}{hc} \Delta\Omega L E_i n_e \frac{\partial\sigma^T}{\partial\Omega} S_{k,\lambda}^M(n_e^M, T_e^M), \quad (3)$$

where $\partial\sigma^T/\partial\Omega$ is the Thomson scattering cross section and η is the system efficiency constant obtained from LRS calibration. Notably, $S_{k,\lambda}^M(n_e^M, T_e^M)$ is a Maxwellian spectral distribution function for Thomson scattering, with

$$\mathbf{x}^M = [T_e^M, n_e^M, v_d]^T \quad \text{and} \quad \boldsymbol{\theta}^M = [\eta, \lambda_i]^T. \quad (4)$$

Section II and the Appendix of Suazo Betancourt *et al.*²³ outline the details of Eqs. (3) and (4).

IV. ANALYSIS OF SPATIALLY RESOLVED ELECTRON PROPERTIES

The LTS measurements described below can be processed to assess how well sheath and presheath models reflect the data. Here, we present the models and how they relate to the measured data.

A. Sheath and presheath length scale estimates

A fluid model for the electron sheath and presheath, as opposed to traditional kinetic models that assumed an interface from the bulk plasma to the electron sheath without an electron presheath, is presented in Ref. 6. The PIC-DSMC simulations agreed well with the fluid model, which used a flowing Maxwellian electron velocity distribution function. Assuming a collisionless sheath, the model estimates the electron sheath size, y_{es} , as

$$y_{es} = 0.79\lambda_{Dc} \left(\frac{e\Delta\phi_{AP}}{k_b T_e} \right), \quad (5)$$

with $\Delta\phi_{AP}$ being the anode to bulk plasma potential, which is a function of the electron Debye length, λ_{Dc} . T_e , k_b , and e are the electron temperature, Boltzmann constant, and electric charge, respectively. Characterizing the electron presheath length y_{eps} by a representative length scale, defined as the ratio of the electron Bohm speed u_{eB} to the electron collision frequency ν_c , yields

$$y_{eps} = \frac{u_{eB}}{\nu_c} = \frac{1}{\nu_c} \sqrt{k_b \left(\frac{T_e + T_i}{m_e} \right)}, \quad (6)$$

where T_i is the ion temperature and m_e is the electron mass.

Estimates of the collisionless ion sheath size, y_{is} , and ion presheath size, y_{ips} , are presented in Refs. 1, 2, and 7 as

$$y_{is} = 0.79\lambda_{Dc} \left(\frac{e\Delta\phi_{CP}}{k_b T_e} \right) \quad (7)$$

and

$$y_{ips} = \frac{u_{iB}}{\nu_c} = \frac{1}{\nu_c} \sqrt{k_b \left(\frac{T_e}{m_i} \right)}, \quad (8)$$

where u_{iB} is the ion Bohm velocity, $\Delta\phi_{CP}$ is the cathode potential with respect to the bulk plasma potential, and m_i is the ion mass. It should be noted that the collisionless assumption for the ion and electron sheaths is not appropriate for this study because of the high neutral densities in the experiment. This inaccuracy motivated the more detailed potential profile estimates in Sec. IV B.

Equations (5) and (7) have the same functional form, with the exception of the potential with respect to the plasma. However, there are several unknown parameters, specifically the potentials with respect to the plasma of the anode and the cathode, the electron and ion temperatures, electron density, and the collision frequency. Because our plasma discharge has a neutral pressure of 6 Torr-Ar, the electron-neutral and ion-neutral collision frequencies are expected to dominate in the electron presheath and ion presheath, respectively.

The electron-neutral collision frequency, ν_{en} , is given by

$$\nu_{en} = n_g \langle \sigma_{en} v_e \rangle \approx \frac{p_g}{k_b T_g} \sigma_{en} \sqrt{\frac{8k_b T_e}{\pi m_e}}, \quad (9)$$

where σ_{en} is the electron-neutral momentum transfer cross section, v_e is the electron thermal velocity, and the brackets indicate an average over the electron velocity distribution. The ion-neutral collision frequency, ν_{in} , is given by

$$\nu_{in} = n_g \sigma_{in} u_{rel} = \frac{p_g}{k_b T_g} \sigma_{in} u_{B}, \quad (10)$$

where σ_{in} is the ion-neutral momentum transfer cross section, and it is assumed that the relative velocity between the ions and neutrals, u_{rel} , is dominated by the ion flow velocity, which is approximated as the ion Bohm velocity.

Creating a stable DC discharge with a number density above the LTS detection limit was not possible due to arcing in the system during these experiments. However, the preliminary measurements of the plasma properties in a lower density, steady DC plasma via a Langmuir probe provided estimates of the electron number density, temperature, and bulk plasma potential with respect to the grounded discharge cell walls. Several Langmuir probe measurements were made at a given DC discharge voltage and neutral background pressure across several species for repeatability of the electron temperature and density measurements. However, uncertainty estimates were not performed using these data. We estimate the potentials with respect to the plasma of the DC electrodes by estimating their potential difference with respect to the ground and subtracting it from the plasma potential differences obtained from the Langmuir probe data, with

$$\phi_{-P} = \phi_{PG} - \phi_{-G}. \quad (11)$$

In Eq. (11), $\Delta\phi_{-P}$, $\Delta\phi_{PG}$, and $\Delta\phi_{-G}$ are the potential of the surface of interest with respect to the plasma, the potential of the plasma with respect to the ground, and the potential of the surface of interest with respect to the ground, respectively. Using these assumptions, the electron length scales are estimated using the ranges presented in Table III.

The electron sheath and presheath length scales are estimated to be on the order of 100 μm and 1 mm, respectively. The ion sheath and presheath lengths are estimated to be on the order of 1 mm and

TABLE III. Sheath size estimate value ranges.

Parameter	Unit	Value range
T_e	(eV)	[0.5,10]
n_e	(m^{-3})	$[1 \times 10^{17}, 1 \times 10^{19}]$
$\Delta\phi_{\text{PG}}$	(V)	[0, 800]
$\Delta\phi_{\text{AG}}$	(V)	[0, V_D]
$\Delta\phi_{\text{CG}}$	(V)	$V_D - \Delta\phi_{\text{AG}}$
V_D	(V)	[1, 20] kV
T_g	(K)	500
p_g	(Torr)	[0.5, 10]
σ_{in}	(m^2)	1×10^{-18} , Ref. 25
σ_{en}	(m^2)	2×10^{-20} , Ref. 26

10 μm , respectively. Analysis of the potential profiles in this region is necessary to determine if the region that traversed close to the electrodes is the presheath region and how this region scales with the discharge voltage.

B. Potential profile estimates

From the 1D sheath theory,²⁷ assumptions of steady-state and cold ions reduce the ion continuity and ion momentum equations to

$$\frac{\partial(n_i u_i)}{\partial y} = n_e v_{iz} \quad (12)$$

and

$$m_i u_i \frac{\partial u_i}{\partial y} = -e \frac{\partial \phi}{\partial y} - m_i v_{\text{in}} u_i - m_i v_{iz} u_i \frac{n_e}{n_i}, \quad (13)$$

where the y component is the axial direction between the electrodes, n_i is the ion number density, u_i is the ion flow velocity, ϕ is the plasma potential, and v_{iz} is the ionization frequency. Only those collisions with slow neutrals were considered. From the electron momentum equation and assuming steady state, negligible electron inertia, collisionless electrons, electrostatic, isotropic thermalized pressure ($p_e = n_e k_b T_e$) closure for the pressure tensor, and spatially isothermal electrons yields the common Boltzmann potential function,

$$n_e = n_{e0} \exp\left(\frac{e\phi}{k_b T_e}\right), \quad (14)$$

where n_{e0} is a reference plasma density away from the sheath where $\phi = 0$.

The system of equations is closed with the electrostatic Poisson equation,

$$-\frac{\epsilon_0}{e} \frac{\partial^2 \phi}{\partial y^2} = n_i - n_e. \quad (15)$$

Equations (12)–(15) are nondimensionalized using the non-dimension variables in Ref. 28,

$$\begin{aligned} s &= \frac{y}{l}, \\ \psi &= -\frac{e\phi}{k_b T_e}, \\ n_{\pm} &= \frac{n_{i,e}}{n_{e0}}, \\ u &= \frac{u_i}{u_B}, \\ v^{\text{in}}(u) &= \frac{v_{\text{in}}(u_i)}{v_{\text{in}}(u_B)}, \\ v^{\text{iz}}(u) &= \frac{v_{iz}(u_i)}{v_{iz}(u_B)}, \end{aligned} \quad (16)$$

where l is a length scale of choice. In this formulation, $s, \psi, n_{\pm}, u, v^{\text{in}}, v^{\text{iz}}$ are the nondimensionalized length, potential, electron and ion number densities, ion velocity, ion-neutral collision frequency, and, finally, ionization frequency. For ion-neutral collisions and electron-impact ionization, the two special cases of constant collision frequency and constant mean free path can be considered.²⁸ Assuming a negligible neutral velocity, the ion-neutral mean free path, λ_{in} , is

$$\lambda_{\text{in}} = \frac{u_i}{n_n \sigma_{\text{in}} u_i} = \frac{1}{n_n \sigma_{\text{in}}}. \quad (17)$$

The neutral pressure of 6 Torr-Ar used to generate the discharge studied in Sec. V results in a neutral density that is significantly larger than the electron density such that the neutral density in Eq. (17) can be assumed to be constant. In addition, with a small change in the ion-neutral momentum transfer cross section between 0.1 and 100 eV of ion beam energy,²⁵ we can assume a constant ion-neutral momentum transfer cross section. As a result, a constant ion-neutral mean free path is a reasonable assumption, leading to $v^{\text{in}}(u) = u$. In addition, assuming that the electrons are isothermal such that $\langle \sigma_{iz} v_e \rangle$ is constant, where σ_{iz} is the electron impact ionization cross section, results in a constant ionization frequency,

$$v_{iz} = n_n \langle \sigma_{iz} v_e \rangle \quad (18)$$

such that $v^{\text{iz}}(u) = 1$. An effective ion ionization mean free path, λ_{iz} , is defined as

$$\lambda_{iz} = \frac{u_i}{n_n \langle \sigma_{iz} v_e \rangle}, \quad (19)$$

which can be interpreted as the length scale below which ionization can be neglected in the ion continuity equation.

The assumptions on collisions and ionization produce a system of ODEs for the nondimensionalized ion momentum,

$$u \frac{\partial u}{\partial s} = \frac{\partial \psi}{\partial s} - \frac{l}{\lambda_{\text{in}}} u^2 - \frac{l}{\lambda_{iz}(u_B)} u \frac{\exp(-\psi)}{n_+}, \quad (20)$$

ion continuity,

$$\frac{\partial(n_+ u)}{\partial s} = \frac{l}{\lambda_{iz}(u_B)} \exp(-\psi), \quad (21)$$

and Poisson equation,

$$\left(\frac{\lambda_D}{l}\right)^2 \frac{\partial^2 \psi}{\partial s^2} = n_+ - \exp(-\psi). \quad (22)$$

The implemented boundary conditions are

$$\begin{aligned} u(0) &= 0.0001, \\ \psi(0) &= 0, \\ \frac{d\psi}{ds}(0) &= 0, \\ n_+(0) &= 1. \end{aligned} \quad (23)$$

Then, the system is iteratively integrated to a domain length that is unknown beforehand until the non-dimensional potential at the end of the domain is a desired non-dimensional wall potential, ψ_w . It should be noted that many simulations^{27,29} have a fixed domain length, L , and replace the $u(0) = 0.0001$ boundary condition with $\psi(L) = \psi_w$. Increasing ψ_w has the same effect as increasing $u(0)$, so there is no physical difference between the two methods.

V. RESULTS

In order to spatially resolve the electron properties between the electrodes, the electrode spacing was held constant, while the

electrodes themselves were translated in the $\pm y$ direction with respect to the laser beam propagation along x using the linear actuators, effectively moving the plasma with respect to the laser beam. As stated previously, the electrodes were spaced 26.5 mm apart. When the laser beam was centered between the electrodes (13.25 mm from each electrode), each electrode actuator was at its 25 mm mark. Spatial profiles of the electron properties were taken by translating the electrodes in 1 mm increments. Note that the measurements were stopped 3.25 mm away from the electrode due to a strong interference from laser reflections off the electrode surfaces.

Data were acquired at a neutral background pressure of 6 Torr-Ar, with the laser pulse delayed by 150 ns with respect to the start of the plasma pulse. Data were acquired at 3.25 mm from the cathode to 26.25 mm from the cathode, denoted as $\Delta y_{b/c}$, at discharge voltages of 20, 16, 12, and 8 kV, respectively. The collection parameters are outlined in Sec. III.

The resulting spatially resolved electron property distributions are presented in Fig. 6.

The sheath model in Sec. IV B is applied to the LTS data to more accurately estimate the expected combined size of the cathode sheath and presheath. The cathode sheath is chosen for comparison because

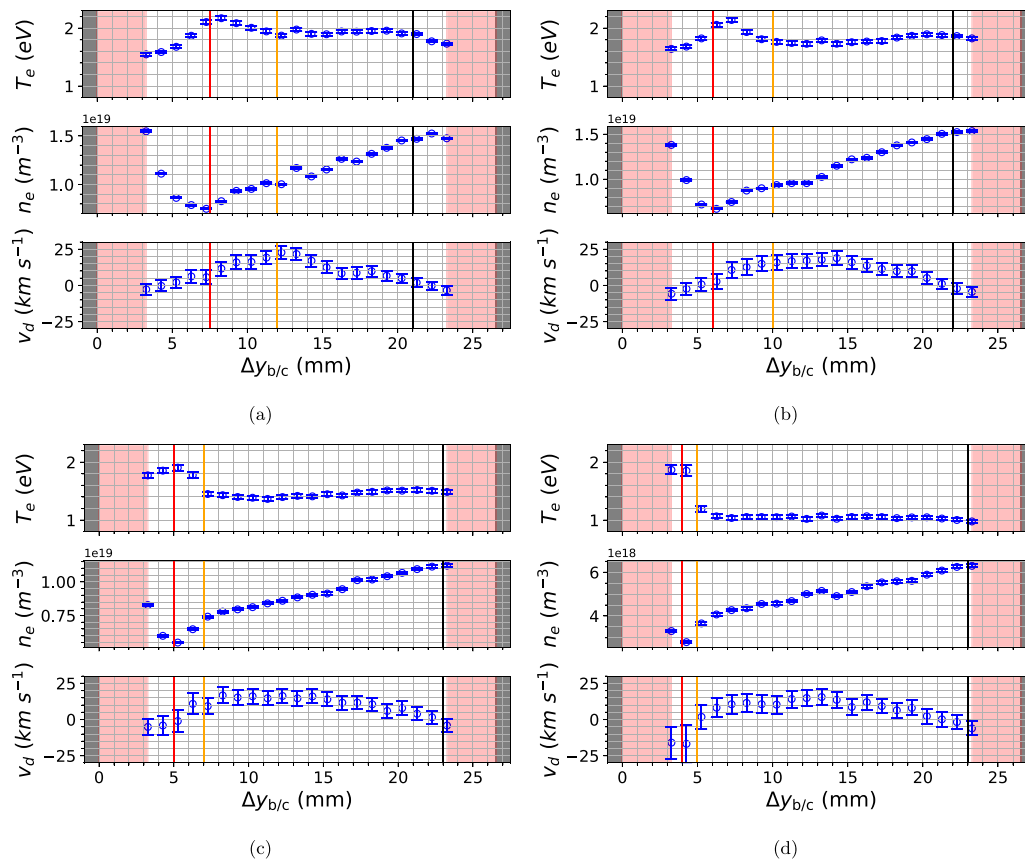


FIG. 6. Spatially resolved electron properties using a Maxwellian (blue) spectral distribution function: (a) 20 kV, (b) 16 kV, (c) 12 kV, and (d) 8 kV. The distance from the cathode to the interrogation beam scattering volume is denoted as $\Delta y_{b/c}$. The electrodes are shaded in gray, and the un-probed regions are in red. The negative glow region is bounded by the left-hand boundary, and the red vertical lines in the figures are defined based on the electron density. The bulk plasma region is bounded by the orange and black lines, which are defined based on the electron temperature. The black and red lines recede toward the boundaries as the voltage is decreased.

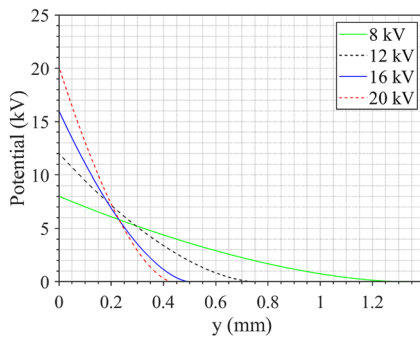


FIG. 7. 1D sheath model applied to the LTS data at 8, 12, 16, and 20 kV. The LTS centerline electron density and electron temperature data are used in the model to evaluate λ_D and $\lambda_{iz}(u_B)$ in Eqs. (20)–(22) and to determine the non-dimensional potential that corresponds to the wall potential.

it is certainly an ion-rich sheath and because the voltage drop across the cathode sheath can be approximated as the discharge voltage. To apply the sheath model to the LTS data, we assume that the temperature of the isothermal electrons in the model is the electron temperature measured at the centerline. The value of n_{e0} is taken as the centerline electron density, and the neutral density is calculated using the neutral pressure and by assuming a neutral temperature of 500 K. The electron-impact single ionization rate at the centerline electron temperature is calculated assuming a Maxwell–Boltzmann speed distribution for the electrons and using data for the electron-impact single ionization cross section for argon.³⁰ The centerline values are chosen from the electron temperature and density data because they are more representative of the trends at different voltages when compared to the data closest to the cathode. The resulting re-dimensionalized potential profile as a function of the distance from the cathode is presented in Fig. 7. The profiles presented are discussed in Sec. VI.

VI. DISCUSSION

This section discusses the visible structures based on the spatially resolved electron properties from the acquired data at several discharge voltages. Then, the joint presheath–sheath model applied to the data is discussed. Finally, the limitations of the system as implemented and future improvements are discussed.

A. Electron property profiles

The profiles in Fig. 6 show characteristic glow discharge structures. A bulk centerline plasma region between 10 and 15 mm at 20 kV, increasing to 6.5–20 mm at 8 kV, suggests the decrease in the near electrode structures and a larger bulk plasma region as the voltage decreases. Decreases in the centerline electron temperature and density in this region are expected with decreasing discharge voltage bias. This decrease in temperature and density is expected because the electrons are expected to be less energetic through a smaller sheath potential drop with decreasing discharge voltage, and as the bulk plasma electron temperature decreases, the ionization frequency is expected to decrease, leading to a smaller electron number density.

The electron Debye length is expected to decrease with decreasing electron temperature. In addition, the increase in the electron density and decrease in electron temperature as the cathode is approached at all voltages indicates the negative glow region in a glow discharge, see Ref. 31. The electron temperature peaks near this negative glow region close to the cathode. This region recedes as the voltage decreases, indicating that the beginning and extent of the negative glow region scales with the voltage as the cathode sheath and presheath recede. This is consistent with the expectations, as the voltage decreases, the necessary space for the potential difference across the sheath and presheath necessary to sustain this discharge voltage also decreases. Given that the negative glow region is expected to be immediately adjacent to the sheath and presheath region, this region will recede as well. The spatial resolution between points of 1 mm was insufficient to determine if the negative glow region also decreases in extent with the discharge voltage.

B. Potential profiles from the applied sheath model

The theoretical potential profiles shown in Fig. 7 indicate a smaller sheath thickness at larger voltages. This observation contradicts the collisionless sheath theory, which states that sheath thickness scaling with the Debye length and voltage drop across the sheath. The same ion-neutral mean free path of $8.6 \mu\text{m}$ was used for all the voltages, but different effective ion ionization mean free paths were used. The effective ion ionization mean free paths were 1.3, 2.9, 19.9, and 515 mm for discharge voltages of 20, 16, 12, and 8 kV, respectively. These ionization mean free paths were calculated using Eq. (19), where $\langle\sigma_{iz}v_e\rangle$ is evaluated assuming a Maxwell–Boltzmann electron velocity distribution. At each discharge voltage, the electron temperature used to evaluate Eq. (19) is the measured electron temperature in the negative glow region closest to the cathode electrode, as shown in Fig. 6. These ionization mean free paths show the importance of ionization in sheaths even when the ion-neutral collision length scale is significantly smaller than the ionization length scale. The calculated combined thickness of the sheath and presheath at the cathode predicted by the model are smaller than the 3.5 mm limit. Given these combined sheath and presheath thicknesses, the generated discharge condition created an expected combined length of the sheath and presheath closer to the cathode than our closest probing point. The combined sheath and presheath thicknesses being closer to the cathode than the closest point probed indicates that the spatial resolution and probed regions are limited in this experiment to resolving the expected glow discharge-like structures and varying plasma parameters. The combined length of the sheath and presheath of the potential profiles matches the order of magnitude estimates from the simplified theory presented in Subsection VI A. Although the 1D sheath theory indicates thinner sheaths for larger voltages, we are not able to probe the sheaths, so we cannot determine whether the increasing extent of the negative glow region for larger voltages is a result of larger sheaths or a larger negative glow region.

C. Spatial resolution limitations and system improvements

Changes of electron density of 50% at a distance of 1 mm and gradients in the electron density approaching the cathode, suggest that the measurement volume resolution approaching the

electrodes, to within a distance of less than 5 mm, must be finer than 1 mm. The measurement volume step must be finer in order to accurately resolve the gradients in electron properties. Finer movement of the interrogation volume can be achieved through a relationship between a turn of the worm gear driving the linear actuators and the engravings on the linear actuator. This is a planned system improvement.

The minimum probing distance of 3.26 mm, which was limited by reflection saturation at the center wavelength and solid angle sub-tension as the electrodes are approached, must be addressed in order to decrease the detection limit. This can be resolved by changing the third lens in the collection optical train to a positive focal length lens and placing a slit at the focal point between the second and third lenses to minimize reflection propagation. In addition, averaging several frames that are on-ccd accumulated after saturation limits the maximum number of accumulations can help improve signal-to-noise ratio. The sub-tension of the collection solid angle as the electrodes protrude into the solid angle cone can be accounted for by collecting spatially resolved LRS close to the electrodes. In addition, the discharge condition trade space must be explored to generate a larger sheath and presheath at the cathode. Decreasing the neutral pressure will increase the presheath thickness. An electron density of $5 \times 10^{16} \text{ m}^{-3}$ and temperature of 5–10 eV will create a thicker sheath. However, the role of discharge voltage is unclear because of the discrepancy between the collisional and collisionless sheath theories.

Finally, the system detection limit must be improved. This can be done by making two simple changes to the system. First, taking advantage of hardware binning over the vertical pixels illuminated by the beam image will increase the signal-to-noise ratio by decreasing read noise. Second, expanding the beam waist diameter via a change in the focal length will allow the full laser energy to be leveraged from the laser. In the current configuration, at a projected peak signal to mean noise ratio of 1, the detection limit is $2 \times 10^{17} \text{ m}^{-3}$. These changes will decrease the detection limit by $5 \times 10^{16} \text{ m}^{-3}$ and possibly below.

VII. CONCLUSIONS

A pressure-controlled discharge plasma cell capable of generating pulsed plasmas with number densities of 1×10^{17} to $1 \times 10^{19} \text{ m}^{-3}$ was developed. A laser Thomson scattering system was developed around this cell in order to study the spatial variation in electron properties perpendicular to the plasma bounding electrodes, in particular in the near cathode region, which is of interest due to the cathode sheath and presheath potential drop.

The combined thickness of the sheath and presheath calculated from the centerline electron properties predicts decreasing thicknesses with increasing discharge voltage; this conflicts with the collisionless sheath theory and merits further study. In order to perform this study, increased spatial resolution and larger expected combined sheath and presheath lengths are required.

The measurement volume step of 1 mm between the electrodes and a minimum electrode probing distance of 3.6 mm proved to be enough to resolve gradients in the electron properties between the bulk plasma and the cathode negative glow region. These represent some of the first laser Thomson scattering measurements with resolution perpendicular to the plasma bounding electrodes in such a

glow-like discharge. However, the relatively high bulk plasma density leads to an expected combined sheath and presheath length of less than the minimum probing point, and therefore, the properties in this region remain unresolved. Small modifications of the cell to decrease the number density detection limit and increasing the resolution in the movement of the interrogation volume are necessary to explore the sheath and presheath regions for model validation.

AUTHOR DECLARATIONS

Conflict of Interest

The authors have no conflicts to disclose.

Author Contributions

Jean Luis Suazo Betancourt: Conceptualization (lead); Data curation (lead); Formal analysis (lead); Investigation (lead); Methodology (lead); Visualization (lead); Writing – original draft (lead); Writing – review & editing (lead). **Julian Lopez-Uricoechea:** Data curation (equal); Formal analysis (equal); Methodology (equal); Visualization (equal); Writing – original draft (equal); Writing – review & editing (equal). **Naia Butler-Craig:** Data curation (equal); Formal analysis (equal); Methodology (equal); Visualization (supporting); Writing – original draft (supporting); Writing – review & editing (supporting). **Adam M. Steinberg:** Funding acquisition (lead); Project administration (lead); Resources (lead); Writing – original draft (equal); Writing – review & editing (equal). **Mitchell L. R. Walker:** Funding acquisition (lead); Project administration (lead); Resources (lead); Writing – original draft (equal); Writing – review & editing (equal).

DATA AVAILABILITY

The data presented in this manuscript are available upon request to the supervisors of this effort, Mitchell L. R. Walker and Adam M. Steinberg.

REFERENCES

- ¹S. J. Langendorf, “Effects of electron emission on plasma sheaths,” Ph.D. thesis (Georgia Institute of Technology, 2015).
- ²N. Hershkowitz, “Sheaths: More complicated than you think,” *Phys. Plasmas* **12**, 055502 (2005).
- ³V. A. Lisovski, K. P. Artushenko, and V. D. Yegorenkov, “Child-Langmuir law applicability for a cathode sheath description of glow discharge in hydrogen,” *Phys. Scr.* **91**, 085601 (2016).
- ⁴P. K. Barnwal, S. Kar, R. Narayanan, R. D. Tarey, and A. Ganguli, “Plasma boundary induced electron-to-ion sheath transition in planar DC discharge,” *Phys. Plasmas* **27**, 012110 (2020).
- ⁵E. V. Barnat, G. R. Laity, and S. D. Baalrud, “Response of the plasma to the size of an anode electrode biased near the plasma potential,” *Phys. Plasmas* **21**, 103512 (2014).
- ⁶B. Scheiner, S. D. Baalrud, B. T. Yee, M. M. Hopkins, and E. V. Barnat, “Theory of the electron sheath and presheath,” *Phys. Plasmas* **22**, 123520 (2015).
- ⁷M. S. Benilov, “The Child-Langmuir law and analytical theory of collisionless to collision-dominated sheaths,” *Plasma Sources Sci. Technol.* **18**, 014005 (2009).
- ⁸I. G. Mikellides, I. Katz, R. R. Hofer, and D. M. Goebel, *Hall-Effect Thruster Simulations with 2-D Electron Transport and Hydrodynamic Ions* (University of Michigan, Ann Arbor, MI, 2009).

- ⁹M. N. Shneider, “Ponderomotive perturbations of low density low-temperature plasma under laser Thomson scattering diagnostics,” *Phys. Plasmas* **24**, 100701 (2017).
- ¹⁰M. Mokrov, M. N. Shneider, and A. Gerakis, “Analysis of coherent Thomson scattering from a low temperature plasma,” *Phys. Plasmas* **29**, 033507 (2022).
- ¹¹S. G. Belostotskiy, R. Khandelwal, Q. Wang, V. M. Donnelly, D. J. Economou, and N. Sadeghi, “Measurement of electron temperature and density in an argon microdischarge by laser Thomson scattering,” *Appl. Phys. Lett.* **92**, 221507 (2008).
- ¹²E. A. D. Carbone, S. Hübner, E. I. Iordanova, N. de Vries, M. Jimenez Diaz, J. M. Palomares Linares, and J. van der Mullen, “Discrepancies between different electron temperature methods: Probing the electron energy distribution function,” in *21st Europhysics Conference on the Atomic and Molecular Physics of Ionized Gases (ESCAMPIG XXI), July 10–14, 2012* (Viana do Castelo, Portugal, 2012), pp. 1–2.
- ¹³E. Carbone and S. Nijdam, “Thomson scattering on non-equilibrium low density plasmas: Principles, practice and challenges,” *Plasma Phys. Controlled Fusion* **57**, 014026 (2014).
- ¹⁴M. A. ElSabbagh, H. Koyama, M. D. Bowden, K. Uchino, and K. Muraoka, “A laser Thomson scattering system for low density glow discharge plasmas,” *Jpn. J. Appl. Phys.* **40**, 1465 (2001).
- ¹⁵K. Muraoka, K. Uchino, and M. D. Bowden, “Diagnostics of low-density glow discharge plasmas using Thomson scattering,” *Plasma Phys. Controlled Fusion* **40**(7), 1221 (1998).
- ¹⁶K. Muraoka, K. Uchino, Y. Yamagata, Y. Noguchi, M. Mansour, P. Suanpoot, S. Narishige, and M. Noguchi, “Laser Thomson scattering studies of glow discharge plasmas,” *Plasma Sources Sci. Technol.* **11**, A143 (2002).
- ¹⁷G. Gamez, A. Bogaerts, and G. M. Hieftje, “Temporal and spatially resolved laser-scattering plasma diagnostics for the characterization of a ms-pulsed glow discharge,” *J. Anal. At. Spectrom.* **21**, 350 (2006).
- ¹⁸J. Bak, J. L. Suazo Betancourt, A. Rekhy, A. Abbasszadehrad, R. B. Miles, C. M. Limbach, and M. L. R. Walker, “High resolution spatially extended 1D laser scattering diagnostics using volume Bragg grating notch filters,” *Rev. Sci. Instrum.* **94**, 023003 (2023).
- ¹⁹B. Vincent, S. Tsikata, S. Mazouffre, T. Minea, and J. Fils, “A compact new incoherent Thomson scattering diagnostic for low-temperature plasma studies,” *Plasma Sources Sci. Technol.* **27**, 055002 (2018).
- ²⁰B. Vincent, “Incoherent Thomson scattering investigations in Hall thruster, planar magnetron and ECR ion source plasmas,” Ph.D. thesis (ICARE—Institut de Combustion, Aérothermique, Réactivité et Environnement, Orleans, 2019).
- ²¹M. J. van de Sande, “Laser scattering on low-temperature plasmas: High resolution and stray light rejection,” Ph.D. thesis (Eindhoven Technical University, 2004).
- ²²A. J. Friss, “Cavity enhanced Thomson scattering for plasma diagnostics,” Ph.D. thesis (Colorado State University, 2019).
- ²³J. L. S. Betancourt, S. J. Grauer, J. Bak, and A. M. Steinberg, “Bayesian model selection for Thomson scattering,” *Revi. Sci. Instrum.* (submitted).
- ²⁴G. A. F. Seber and C. J. Wild, *Nonlinear Regression* (John Wiley & Sons, New Jersey, 2003), Vol. 62, pp. 21–30.
- ²⁵A. V. Phelps, “Cross sections and swarm coefficients for nitrogen ions and neutrals in N₂ and argon ions and neutrals in Ar for energies from 0.1 eV to 10 keV,” *J. Phys. Chem. Ref. Data* **20**, 557–573 (1991).
- ²⁶M. Suzuki, T. Taniguchi, and H. Tagashira, “Momentum transfer cross section of argon deduced from electron drift velocity data,” *J. Phys. D: Appl. Phys.* **23**, 842 (1990).
- ²⁷M. Keidar and I. I. Beilis, “Transition from plasma to space-charge sheath near the electrode in electrical discharges,” *IEEE Trans. Plasma Sci.* **33**, 1481 (2005).
- ²⁸K.-U. Riemann, “The influence of collisions on the plasma sheath transition,” *Phys. Plasmas* **4**, 4158–4166 (1997).
- ²⁹I. D. Kaganovich, “How to patch active plasma and collisionless sheath: A practical guide,” *Phys. Plasmas* **9**, 4788 (2002).
- ³⁰R. Rejoub, B. G. Lindsay, and R. F. Stebbings, “Determination of the absolute partial and total cross sections for electron-impact ionization of the rare gases,” *Phys. Rev. A* **65**, 042713 (2002).
- ³¹A. Fridman, *Plasma Chemistry* (Cambridge University Press, 2008), Chap. II, pp. 12–89.